Composite Structures 381 (2026) 120024

Contents lists available at ScienceDirect

Composite Structures

journal homepage: www.elsevier.com/locate/compstruct

Steering for in-situ AFP-manufactured structures: Part 2 - Optimized layup strategy

Lukas Raps *, Ashley R. Chadwick, Yannick Schäfer, Heinz F. Voggenreiter

German Aerospace Center (DLR) - Institute of Structures and Design, Pfaffenwaldring 38-40, Stuttgart, 70569, Germany

ARTICLE INFO

Keywords:
Automated Fiber Placement
In-situ consolidation
Thermoplastic composites
Steering

ABSTRACT

Thermoplastic Automated Fiber Placement (AFP) steering enables the fabrication of complex curved structures, but requires careful control of tape geometry to avoid defects. This paper details a methodology for constant curvature steering based on an empirical model characterizing tape deformation during in-situ AFP. A corresponding path planning algorithm leverages this model to generate defect-free steered plies. The approach was experimentally validated for both half-inch and quarter-inch tapes, demonstrating robustness across different process parameters and material combinations. Results show that quarter-inch tape offers a wider design space for steering applications than half-inch tape. By combining the critical arc length concept introduced in Part 1 of this work with steering-optimized path planning, this paper establishes a framework for process-optimized layup strategies to manufacture high-quality in-situ AFP structures.

1. Introduction

Carbon-fiber-reinforced polymer composites are increasingly utilized in primary aircraft structures, driving demand for scalable manufacturing solutions beyond traditional autoclave consolidation and mechanical fastening. Thermoplastic composites, coupled with Automated Fiber Placement (AFP), offer a promising route to Out-of-Autoclave (OoA) processing and large-scale production. While recent advancements in AFP-grape prepreg materials and temperature controlled laser heating technology have enabled near-press consolidation quality in flat thermoplastic AFP panels [1], realizing the potential for complex, double-curved geometries remains a significant challenge. Part 1 of this series established critical arc length parameters defining the usable design space for steered thermoplastic tapes during in-situ AFP. This second part builds on those findings by investigating the resulting course of the consolidated tape geometry of steered tapes following the AFP process. Understanding and predicting the geometry is crucial for developing optimized layup strategies that mitigate defects such as gap defects between narrowing steered tapes and ensure high laminate quality. This research details the characterization of these dimensional variations and presents a framework for informed layup optimization in complex thermoplastic AFP applications.

A detailed overview of thermoset and thermoplastic AFP steering literature is presented in Part 1 of this work, discussing steering radius limits for respective tape widths and otherwise occurring steering-induced defects. The following is a brief overview of strategies that have already been presented in the literature to optimize the layup of steered plies. Subsequently, the thermoplastic steering literature on geometric changes over curved paths is specifically discussed as a basis for this work.

1.1. Layup strategies for steering

For thermoset AFP, the state of the art is based on critical steering radii. Smaller radii are not used in order to avoid out-of-plane defects [2–5]. Geometric changes in tape width and thickness are relatively small due to the large radii and residual gap defects between curved tapes are minimized in the subsequent autoclave consolidation, leaving at most matrix-rich regions but no pores in the laminate.

Kim et al. [6–9] introduced a tow-shearing approach (Continuous Tow Shearing) that combines dry-fiber tape with semi-impregnation by a resin film. This technique eliminates steering-induced, gap and overlap defects. In their implementation the end-effector moves only translationally instead of rotationally, shearing the tape rather than bending it. The method achieves a markedly reduced minimum steering radius, reported as low as 30 mm. However, the total steering angle must be kept below 90° and an equivalent curved segment in the opposite direction is required to restore the tow geometry.

* Corresponding author.
E-mail address: lukas.raps@dlr.de (L. Raps).

https://doi.org/10.1016/j.compstruct.2025.120024
Received 15 June 2025; Received in revised form 22 December 2025; Accepted 30 December 2025
Available online 8 January 2026

Table 1
Thermoplastic AFP dimensional changes with varying steering radii for 6.35 mm prepreg tape.

Steering radius [mm]	Width change [%]		Thickness change [%]	
	[11]	[12]	[11]	[12]
1000	–	−3.8 ± 0.6	–	29.1 ± 2.0
800	−4.8 ± 1.0	−2.7 ± 0.4	5.5 ± 2.6	34.0 ± 3.2
600	−10.9 ± 3.1	−3.4 ± 0.4	9.7 ± 2.6	44.4 ± 3.1
400	–	−5.0 ± 0.4	–	50.9 ± 2.4
200	−16.4 ± 1.9	−9.0 ± 0.5	17.1 ± 3.3	86.1 ± 1.8

1.2. Thermoplastic steering - dimensional changes

The literature on thermoplastic steering has analyzed the change in consolidated tape geometry as a result of steering. These geometrical distortions were observed in part applications, with gaps forming between narrowing steered tapes during the manufacture of complex structures such as a wingbox [10,11].

A consistent finding across studies is that steering induces dimensional changes, specifically a narrowing of the tape width and an increase in thickness, with the severity of these changes directly correlated to the steering radius. Rajasekaran and Shadmehri [12] demonstrated this effect using hot gas torch heating AFP, observing a reduction in tape width from 9.65 mm to 8.79 mm and an increase in thickness from 0.10 mm to 0.19 mm at a 200 mm steering radius. Similarly, Clancy et al. [11] found a 1.22 mm width reduction and 0.09 mm thickness increase at the same radius using diode laser heating AFP. These changes are attributed to stresses induced during steering, leading to defects like fiber wrinkling, pull-up, buckling and folding. Zenker and Gnaedinger [13] further observed gap formation in AFP processes, demonstrating a direct relationship between tighter steering radii and increasing gap areas between tapes layed up in parallel.

The narrowing and thickening effects were considered within the stationary state of steering without considering the transition from straight to curved layup paths. Constant width and thickness values were therefore determined for the respective radii. An overview of the literature results is shown in Table 1.

In part 1 of this paper, however, a continuously decreasing tape width with a simultaneously increasing variance of the tape width up to the occurrence of critical out-of-plane defects was observed. Furthermore, a proportional correlation was found between the steering radius and the consolidated tape width at the critical arc length.

1.3. Novelty

While prior research has identified tape narrowing following steering, these studies largely focused on stationary steering effects. This work addresses a critical research gap by investigating the transient dimensional changes of steered tapes, starting with straight lead-ins representative of realistic layup paths. An extension of the critical arc length principle to quarter-inch tape widths is introduced and a data-based model for accurately predicting tape edge positions, enabling the development of defect-free steering strategies for in-situ AFP is presented.

2. Analytical considerations for geodesic curvature and in-situ AFP

Existing steering models for AFP largely focus on fully steered paths, neglecting the transition region between straight lead-in and steered segments. These models typically assume an infinite steering radius, effectively assuming constant strain throughout the steered path, as illustrated in Fig. 1(a) [14,15].

The compressive strain at the inner edge of the tape, ε_c, is often calculated based on the steering radius and tape width (w_t) using Eq. (1) [14,15]:

$$\varepsilon_c = \frac{w_t}{R + \frac{w_t}{2}} = \frac{1}{\frac{1}{K_g w_t} + \frac{1}{2}} \tag{1}$$

where K_g represents the geodesic curvature and the outer edge is used as the strain reference under the assumption of pure bending deformation of the tape.

In contrast to this established approach, this work introduces a novel approach that accounts for the progressive development of steering-induced stresses and strains. The transition from a straight lead-in to a section with constant curvature is considered, allowing for a gradual increase in deformation. Fig. 1(b) depicts this progression, visualizing the steering-induced length difference, $\Delta l(\alpha_{arc})$, as a function of arc length along the steered path. Utilizing the local tape width parameter, ρ_w, ranging from 0 to w_t (as defined by Zenker [14]), the progressive length difference is calculated as follows:

$$\Delta l(\alpha_{arc}, \rho_w) = (R + \frac{w_t}{2})\alpha_{arc} - (R + \frac{w_t}{2} - \rho_w)\alpha_{arc} = \rho_w \alpha_{arc} \tag{2}$$

where α_{arc} represents the arc angle in radians.

The strain distribution resulting from this progressive length difference is dependent on the tape's deformation characteristics. Results in Part 1 suggest that stresses increase along the steered path, indicating that the total length difference is not entirely accommodated by localized strain in the tape material. Three modeling approaches are considered below – no tape deformation, complete bending deformation, and complete shear deformation – recognizing that the actual deformation mechanism will likely represent a combination of these scenarios.

For the first case the stress distribution in the tape during steering is modeled assuming negligible tape deformation. Under this assumption, the entire length difference induced by steering is transferred to the incoming tape. Assuming a linear elastic material response, the compressive stress increases linearly along the steered path. In simplified terms, the strain can be calculated as the ratio of the length difference to the free length of the incoming tape l_f between the consolidation roller and the tape guiding system. Considering an initial tensile stress, σ_0, the stress distribution is given by:

$$\sigma(\alpha_{arc}, \rho_w) = \sigma_0 - \frac{\rho_w \cdot \alpha_{arc}}{l_f} E_c \tag{3}$$

where E_c is the linear elastic compressive modulus of the tape and the initial stress is related to the tape force, F_t, thickness, t_t, and width, w_t, by:

$$\sigma_0 = \frac{F_t}{w_t \cdot t_t} \tag{4}$$

The resulting stress distribution, dependent on initial tape tension, steering radius, and the compressive modulus, is illustrated in Fig. 1(c).

The initial uniform tensile stress is progressively superimposed with the steering-induced compressive stress. At some point along the inner edge, the compressive stress exceeds the tensile stress, causing the neutral fiber to shift towards the outer edge. Tensile stress generates a force towards the consolidation roller, while compressive stress generates an opposing force, enabling the tape to bend away from the roller.

This model uses the assumption that no additional tensile stress is exerted on the outer tape edge fibers and the neutral fiber thus shifts towards the outer edge of the tape. Zenker et al. showed that the neutral fiber shifted to around 1 mm from the outer tape edge for quarter-inch tape and 1000 mm steering radius [16], indicating that these assumptions are reasonable.

Two extreme cases of tape deformation can be contemplated to describe the actual deformation. The first is complete bending deformation, where the entire length difference is accommodated by in- and out-of-plane fiber undulations, theoretically maintaining a constant

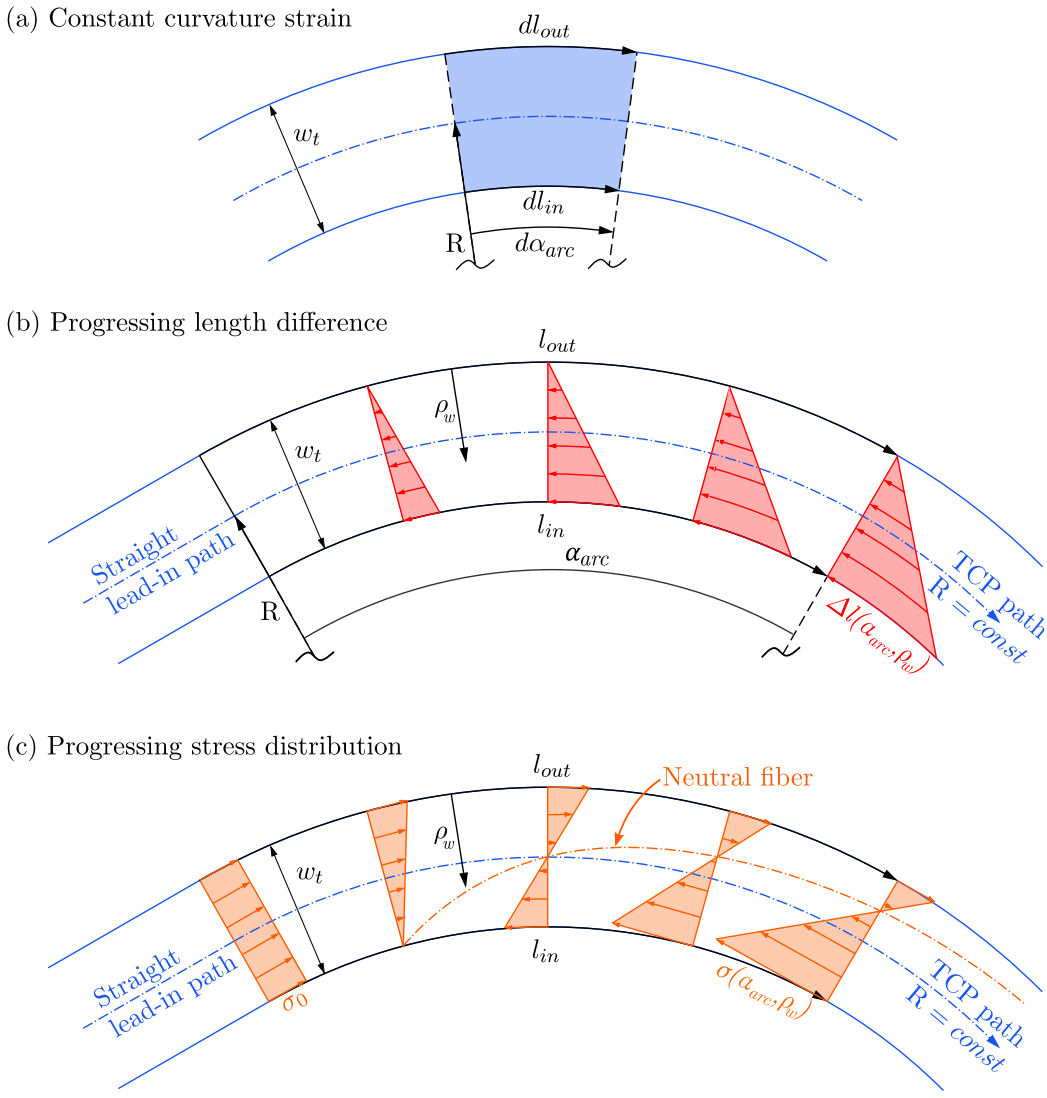

Fig. 1. Analytical derivation of stress distribution for a constant curvature steered path with a straight lead-in: (a) Constant curvature strain [14,15], (b) Progressing length difference, (c) Progressing stress distribution considering initial tape tension and steering.

tape width and compressive bending strain ε_c at the inner tape edge (Fig. 2(a)).

The second theoretical case is complete shear deformation, where the inner and outer tape edges remain the same length and thus fibers are not subject to tensile or compressive strain but the entire deformation takes place in the form of matrix shear. The radius of the inner and outer edge are equivalent to the reference steering radius R. The resulting shear strain γ (Fig. 2(b)) can be calculated for $w_t \ll R$ following:

$$\gamma(\alpha) = \frac{\sin(\alpha) \cdot w_{t,0}}{\alpha \cdot R} \tag{5}$$

where α is the arc angle and $w_{t,0}$ is the tape width at the beginning of the steering radius. The shear-induced reduction in tape width $w_t(\alpha)$ can be calculated for $w_t \ll R$ following:

$$w_t(\alpha) = \cos(\alpha) \cdot w_{t,0} \tag{6}$$

Theoretically, at $\alpha = 90\,\text{deg}$ the tape width becomes 0 and the strain approaches $\frac{2 \cdot w_{t,0}}{R}$. This shear deformation mode is utilized in Continuous Tow Shearing (CTS) technology, employing a translational path and dry fiber tape with a lead section to enable significant relative shearing [6].

The described considerations are useful to describe the basic deformation mechanisms and to visualize the progressively increasing stresses over the course of the steered path. In real thermoplastic Automated Fiber Placement (AFP) processes, however, only a short lead section of partly melted tape in front of the consolidation roller enables localized bending or shear deformation. The laser heat source targets primarily the lower surface of the tape, whereas most of the cross-section of the tape remains below the melting temperature. The transient bending and shear stresses combined with steep temperature gradients in tape length and thickness direction with associated resin viscosities result in a complex transient three-dimensional thermomechanical correlation. For this reason, an empirical model based on experimental results is proposed in this paper.

3. Methodology

3.1. Manufacturing facility and parameters

The Automated Fiber Placement (AFP) experiments were performed using the thermoplastic tape placement facility at the German

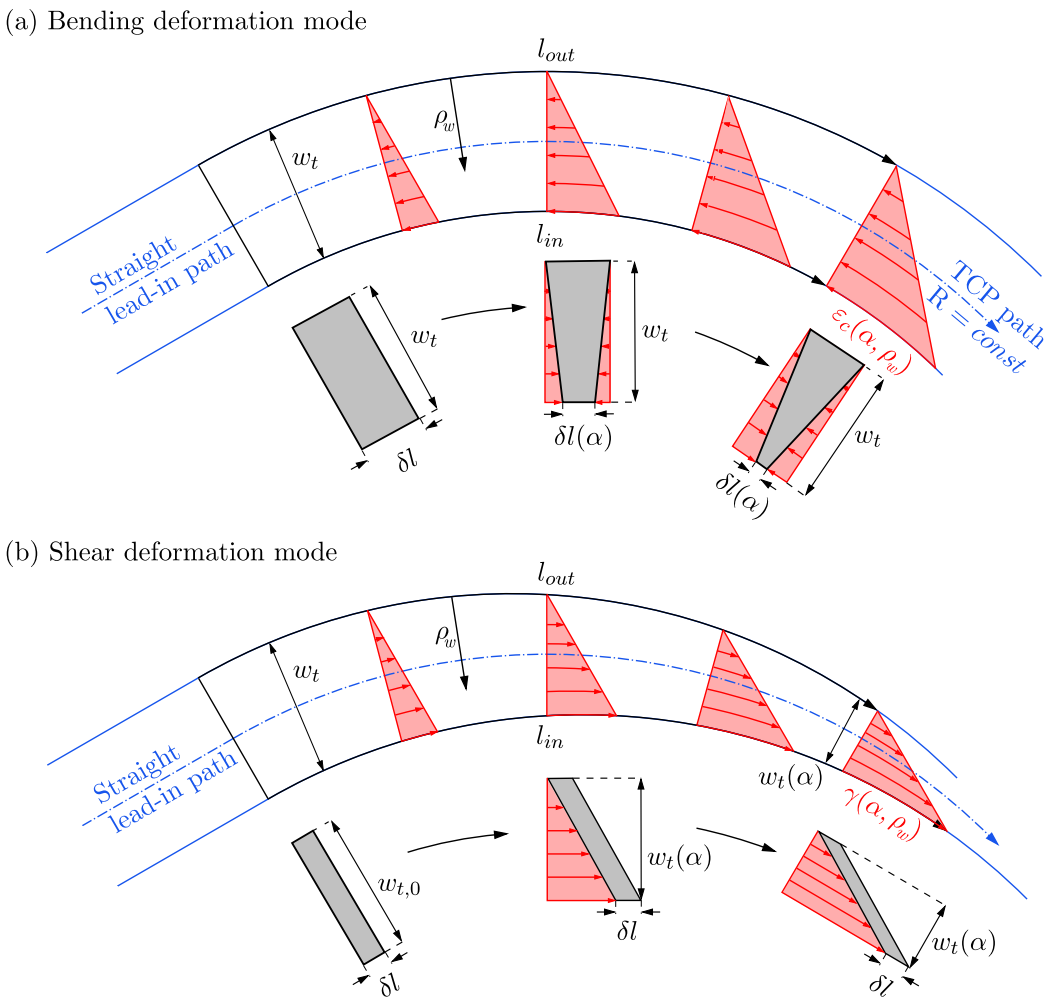

Fig. 2. Steering stress-induced tape deformation modes.

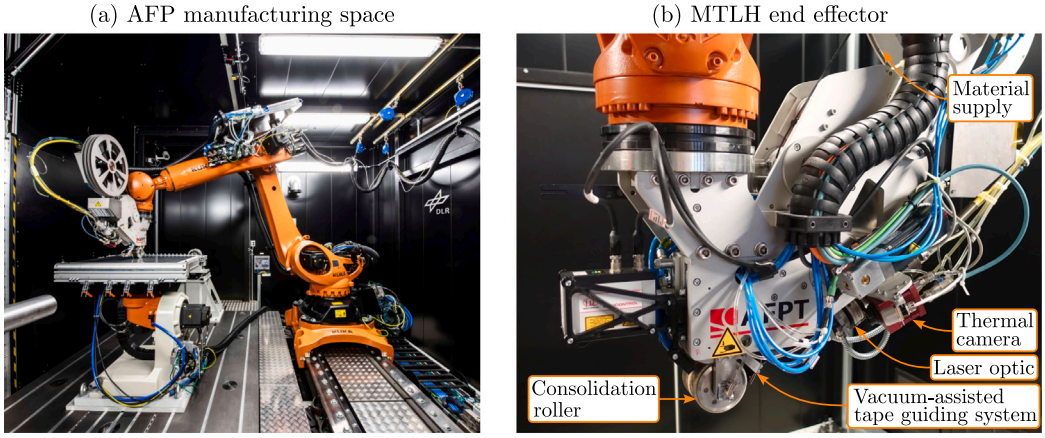

Fig. 3. Thermoplastic tape placement facility.

Aerospace Center (DLR) - Institute of Structures and Design, as described in Part 1 (Fig. 3). This facility consists of a six-axis industrial robot, a two-axis positioner, and flat, heatable aluminum tooling. A multi tape laying head (MTLH) end-effector (AFPT GmbH, Doerth, Germany) was employed to process up to three 12.7 mm wide thermoplastic tapes. Consolidation was achieved using a water-cooled steel roller (60 mm width, 80 mm diameter) with a 5 mm thick outer layer of 60 Shore A silicone, applying a 500 N compaction force. A vacuum-assisted tape guiding system, developed in-house at DLR, was implemented for enhanced layup accuracy. Single tow layup was performed utilizing a 6 kW near-infrared diode laser heat source (Laserline GmbH, Muelheim-Kaerlich, Germany) and OTS-1 optics, generating a 43 mm × 11 mm focal spot for 6.35 mm wide tape and a 40 mm × 20 mmm focal spot for 12.7 mm wide tape at a working distance of 195 mm and 242 mm, respectively. Substrate and tape surface temperatures were continuously monitored via an infrared sensor array,

Table 2
AFP manufacturing parameters [17].

Layup speed [mm/s]	125
Consolidation force [N]	500
Tool set temperature [°C]	20
Nip point set temperature [°C]	470
Tape tension [N]	15

Table 3
Steering radii iterations and corresponding tape width.

R [mm]	12.7 mm tape iterations	6.35 mm tape iterations
4000	3	–
3500	3	–
3000	3	–
2500	3	6
2250	–	6
2000	3	9
1750	–	9
1500	9	9
1250	6	9
1000	11	9
750	6	9
500	6	9
250	–	6

forming a closed-loop control system to regulate laser power and incidence angle. The utilized process parameter set, established through prior research and detailed in Table 2 [17], remained consistent with the methodology outlined in Part 1. AFP-grade CF/LM-PAEK prepreg tape (Suprem SA, Yverdon-les-Bains, Switzerland) with 55% fiber volume fraction, 6.35 mm and 12.7 mm tape width and 0.13 mm and 0.19 mm unprocessed tape thickness, respectively was used for the experiments to evaluate the impact of tape width on steering results.

Hot pressed substrate laminates were fabricated to provide a smooth surface suitable for accurate detection of consolidated tape edges via the optical 3D measuring system. The laminates employed a [45/−45/90/0/−45/45/0/90/−45/45] ply stacking sequence and utilized 300 mm CF/LM-PAEK prepreg tape. Fabrication was performed using a Dieffenbacher GmbH (Eppingen, Germany) HPO 400 hot press.

3.2. Steering experiments and analysis

Steering performance was investigated using straight lead-in paths followed by constant steering radii ranging from 1500 mm to 250 mm, using the standard unheated tooling AFP process parameters. Due to limitations observed in Part 1 experiments, the 250 mm radius was investigated only with quarter-inch tape, while radii greater than 2500 mm were investigated only with half-inch tape, as these larger radii are not critical for quarter-inch tape. The tested radii for each tape width are detailed in Table 3.

The critical arc length (l_{crit}), as introduced in Part 1, was measured for all manufactured steering tracks. Tape dimensions and layup paths were characterized using a Carl Zeiss GOM Metrology GmbH (Braunschweig, Germany) ATOS 5 optical 3D scanning system. Curves representing the tape edges were constructed along the steered tape using GOM Inspect 2020 software to generate 3D point clouds and surface models. The edge position was determined up to the point where the first out-of-plane defect reached the inner tape edge. Due to the flattened edge shape observed in the scan data (Fig. 4(a)), the edge position was defined as the point of maximum curvature, detectable automatically by the evaluation software. Tape width and center were calculated using a MATLAB script. For each point on the inner radius curve, the script iterated through points on the outer radius and calculated the corresponding distances. The local tape width was defined as the minimum calculated distance, and the local tape center was subsequently calculated by adding half the local tape width vector to the inner radius point (Fig. 4(b)). Data visualization and statistical

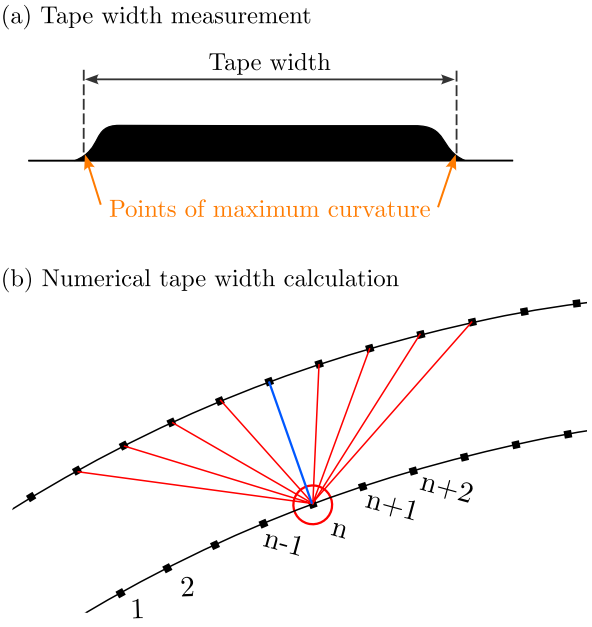

Fig. 4. Optical 3D scan analysis of steering experiments.

analysis were then performed using Python, leveraging the NumPy, pandas, statsmodels, SciPy, Matplotlib, and seaborn packages.

To quantify steering performance, the consolidated tape geometry data was transformed to the global coordinate system of the AFP facility using a Python script. This allowed for superposition of tracks with identical radii to analyze geometrical variance. The measured tape geometry was then compared to both CAD-derived path planning data and real-time Tool Center Point (TCP) data recorded by the facility's data acquisition system.

Bivariate spline functions (SciPy 1.15.1 `SmoothBivariateSpline`) were fitted to the average inner and outer tape edge curves across multiple steering radii. A model was then developed to optimize subsequent track placement by minimizing the distance between the outer edge of a given track and the inner edge of the subsequent track. Optimization was constrained by fixed x-coordinates for steering start points and constant geodesic curvature. Initial analysis indicated negligible optimization potential via x-direction shifting; therefore, the radial distance between tape edges integrated over the arc length served as the primary optimization variable. The solution was determined numerically, iteratively refining subsequent steering tracks starting from a nominal baseline.

The model was validated using example plies of both half- and quarter-inch tape widths, initiated with a 1500 mm radius. Straight 65 mm lead-in and 120 mm track-end segments were added to the steered paths derived from the optimization model. These example plies were again laid up on hot-pressed substrate laminates using process parameters consistent with previous steering experiments, and resulting geometry was assessed via the same optical 3D scanning method.

4. Results and discussion

4.1. Optical 3D measurement results

As established in Part 1, a correlation between steering radius and defect onset was also observed in the expanded out-of-plane defect dataset for quarter-inch and half-inch tape (Fig. 5). Larger steering radii resulted in longer arc lengths without out-of-plane defects (critical arc length). The critical arc length (l_{crit}), at which defects initiated,

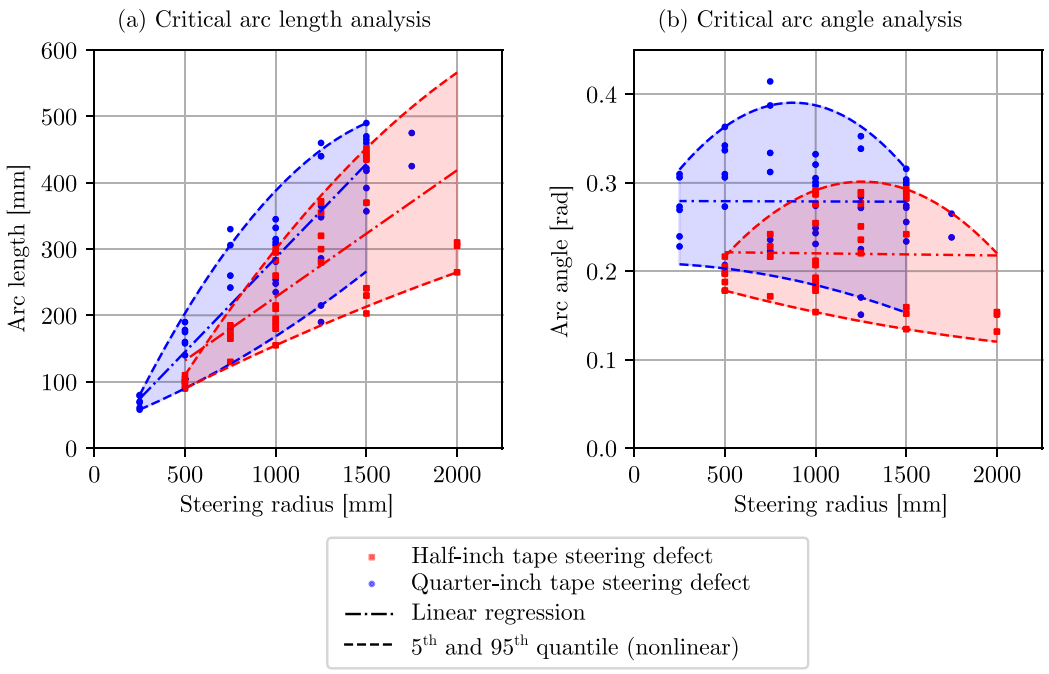

Fig. 5. Critical arc length and arc angle analysis for onset of out-of-plane defects with hot-pressed substrate.

is plotted in Fig. 5(a), while Fig. 5(b) illustrates defect onset relative to the arc angle (α_{arc}). Steering radii exceeding 1500 mm and 2000 mm for quarter-inch and half-inch tape, respectively, did not consistently produce out-of-plane defects within the investigated arc length; radii of 3500 mm and above exhibited no defects for half-inch tape, and 2000 mm and above for quarter-inch tape. These radii were considered non-critical for the respective tape widths, and were excluded from subsequent statistical analysis. Linear regression analysis yielded comparable root mean square error (RMSE) values to higher-order polynomial or spline fits, supporting a linear relationship between steering radius and critical arc length, as observed in the initial experiments in Part 1. The resulting linear curve fits in Fig. 5(b) indicate a consistent arc angle limit for defect initiation, independent of steering radius. Average arc angles of 0.22 rad and 0.28 rad were observed for half-inch and quarter-inch tape, respectively. The inter-quantile range of 90% demonstrates significant variation in defect onset. A conservative upper arc angle limit of the 5% percentile is proposed for the steering-optimized layup strategy in the following work to minimize the occurrence of out-of-plane defects.

Representative steered and straight reference tracks as were used as the basis for the 3D measurement and data-based evaluation of the tape edges are shown in Fig. 6(a). Analysis of the half-inch reference tracks (Fig. 6(b)) revealed minor fluctuations in consolidated tape width (14.47 ± 0.22 mm) in the quasi-stationary parts of the tracks between 100 mm and 300 mm track length. Quarter-inch tape exhibited a consolidated width of 8.48 ± 0.27 mm, representing a proportionally larger increase (33.5%) compared to the half-inch material (13.9%), along with greater width variance. The edge analysis of the quarter-inch data thus generally shows a significantly higher variance of the tape width, which aggravates the accurate prediction and modeling of the edge curves and must be taken into account for the following analysis of the curved tapes.

The analysis of the 3D measurement data of the curved tapes is shown in Figs. 7 and 8. Fig. 7 presents measured tape edges, tool center point (TCP) trajectories, and planned path centerlines (CAD) for half-inch tracks with steering radii of 1000 mm, 1250 mm, and 1500 mm, following straight lead-in sections. To visualize the resulting consolidated tape geometries, individual measured tape edges and calculated centerlines were projected onto a common reference position.

There was no measurable difference found between the CAD-derived path centerlines and the recorded TCP trajectories, indicating accurate path execution. Theoretical CAD tape edges were generated as parallel lines offset from the centerline by half the consolidated tape width, representing the theoretical complete bending deformation. The differing x and y-axis scaling was applied to enhance visualization of the deformation effects, resulting in an apparent convergence of the parallel lines.

While the steering arc began at $x = 0$ mm, deviations between the measured and CAD tape edges were observed in the preceding straight lead-in section. Detail view A reveals an inward shift of both the measured tape edges and centerline relative to the CAD reference, with the tape width remaining constant. Conversely, detail view B, at a larger steering arc length, demonstrates a narrowing of the consolidated tape width. The inner edge closely followed the CAD tape edge, while the outer edge exhibited an inward shift towards the centerline. Furthermore, undulations were observed along the measured inner edge, contributing to increased variance in its position. The acting forces thus initially deflect the tape inwards from the theoretical path, starting before the steering radius. As the consolidated tape width does not change here, the geometry is similar to the bending deformation described above. The tape becomes narrower over the course of the steered path, with the inner edge following the theoretical path and the outer edge shifting further inwards. The narrowing of the tape and the shear defects that occur towards the critical arc length suggest that a shear deformation mode is also present in this progressed steering section. The clearly visible in-plane undulations at the inner tape edge confirm literature findings that the compressive stress at the inner edge is compensated by buckling of the fibers.

Fig. 8 presents the analogous analysis for quarter-inch radii tracks. As observed in the straight-width analysis, the steered quarter-inch tracks exhibited a larger variance in tape edge positions. While detail view A reveals a similar inward shift of the tape edges at the start of the steering arc, a pronounced narrowing or deviation of the outer tape edge from the theoretical CAD curve in detail view B was not observed. Overall, the greater variance in tape width and edge positions complicate a clear interpretation of the results. The larger variance may be attributed to the reduced directional stability of the thinner and narrower quarter-inch tape. Additionally, the vacuum-assisted tape

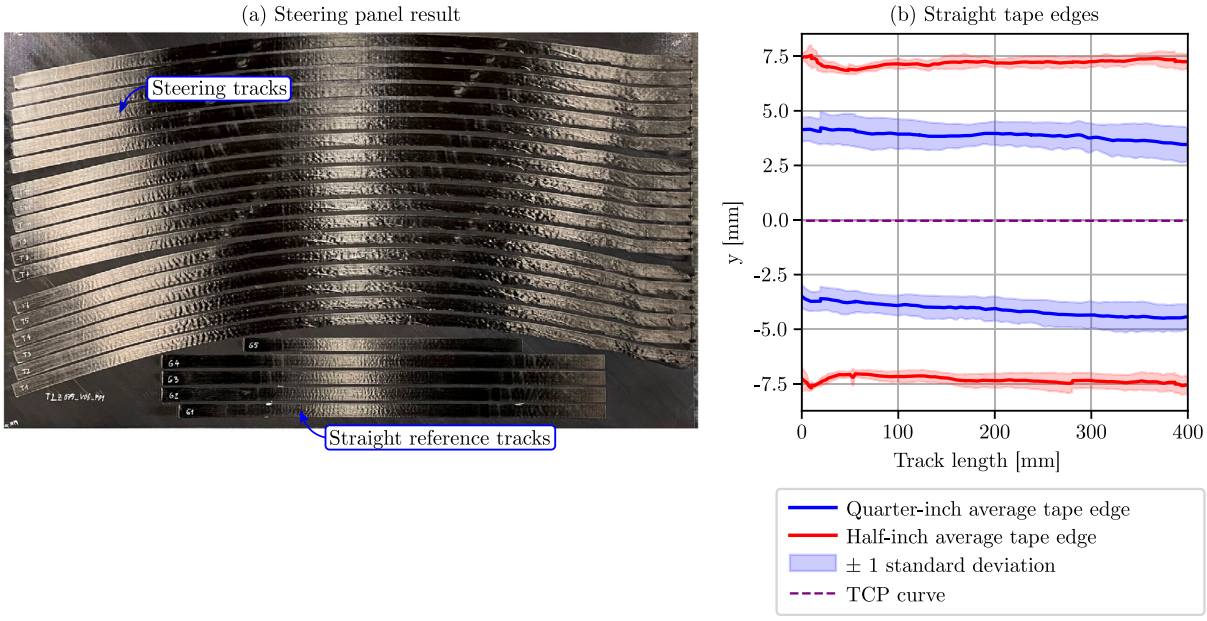

Fig. 6. Resulting steering panel and analysis of straight half-inch reference tracks.

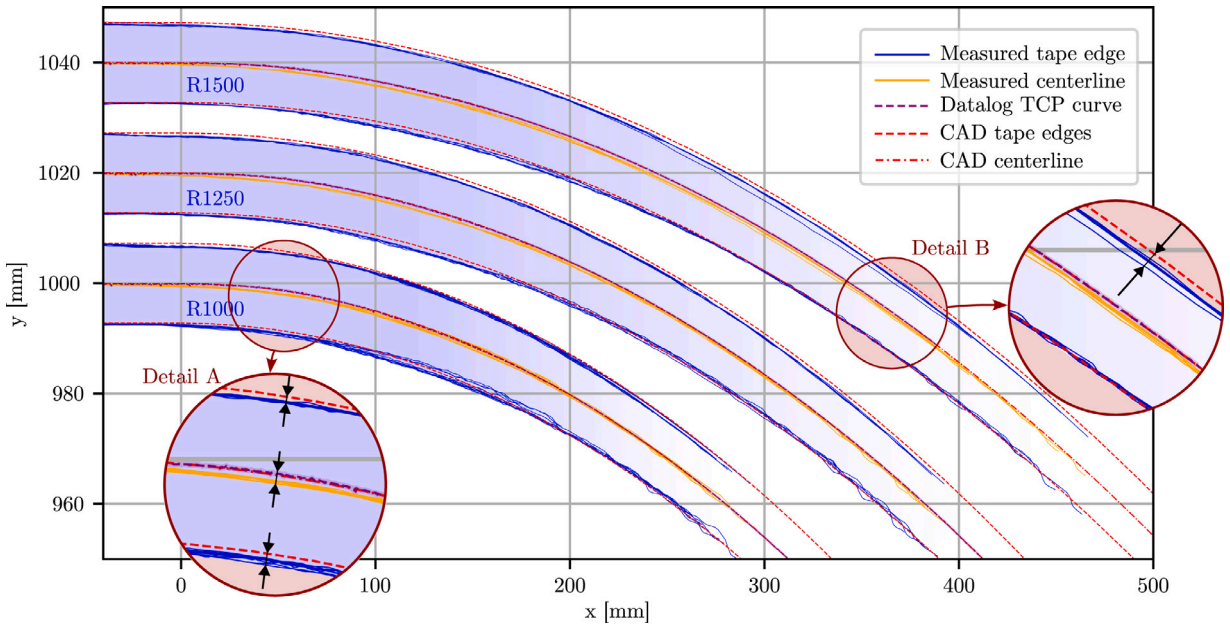

Fig. 7. Optical 3D scan analysis results for superimposed 1500 mm, 1250 mm and 1000 mm steering radii with half-inch tape.

guiding system was optimized for half-inch tape and allowed for more lateral movement of the quarter-inch tape as it can exert less transverse force due to the smaller contact area of the narrower tape and lower resulting vacuum contact pressure. One aspect of future work will be the optimization of the tape guiding system for narrower tapes in order to optimize these results.

4.2. Data-based optimized layup strategy

From the measured geometrical data, an empirical model was developed to predict consolidated tape edges, enabling selection of optimal steering radii to minimize gaps. For each experimentally analyzed steering radius, median curves for the respective inner and outer tape edges were derived from the superimposed tape edge curves. To increase the accuracy of the model, the radial distance between the theoretical centerline and the inner and outer edges of the tape were used as input values. The model, visualized in Fig. 9, extends the tape edge distance curves with a steering radius dimension, creating bivariate spline fits for both outer and inner edges (Fig. 9(a) and (b)). The fitting parameters are listed in Table 4 and the complete set of knot vectors and B-spline coefficients is attached in the Appendix. The smoothing factors were chosen empirically to balance overfitting and underfitting. The residuals had standard deviations of 0.04 mm to 0.1 mm and maximum values of 0.15 mm to 0.38 mm, indicating a good fit as these values are within the width variance of the straight reference tracks.

Transforming these splines to cartesian coordinates yields three-dimensional spline functions, which can be used to predict steered track edges within the range of the measured dataset (Fig. 9(c) and (d)).

As described in the methodology section, the empirical optimization algorithm minimized the integral of the radial distance between the

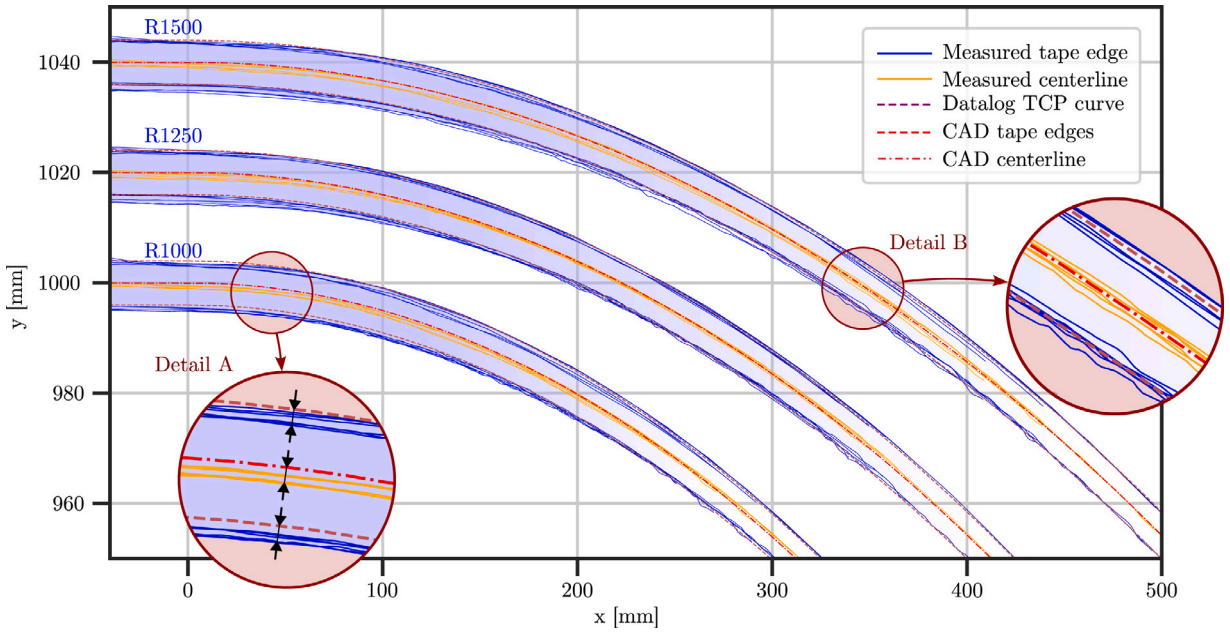

Fig. 8. Optical 3D scan analysis results for superimposed 1500 mm, 1250 mm and 1000 mm steering radii with quarter-inch tape.

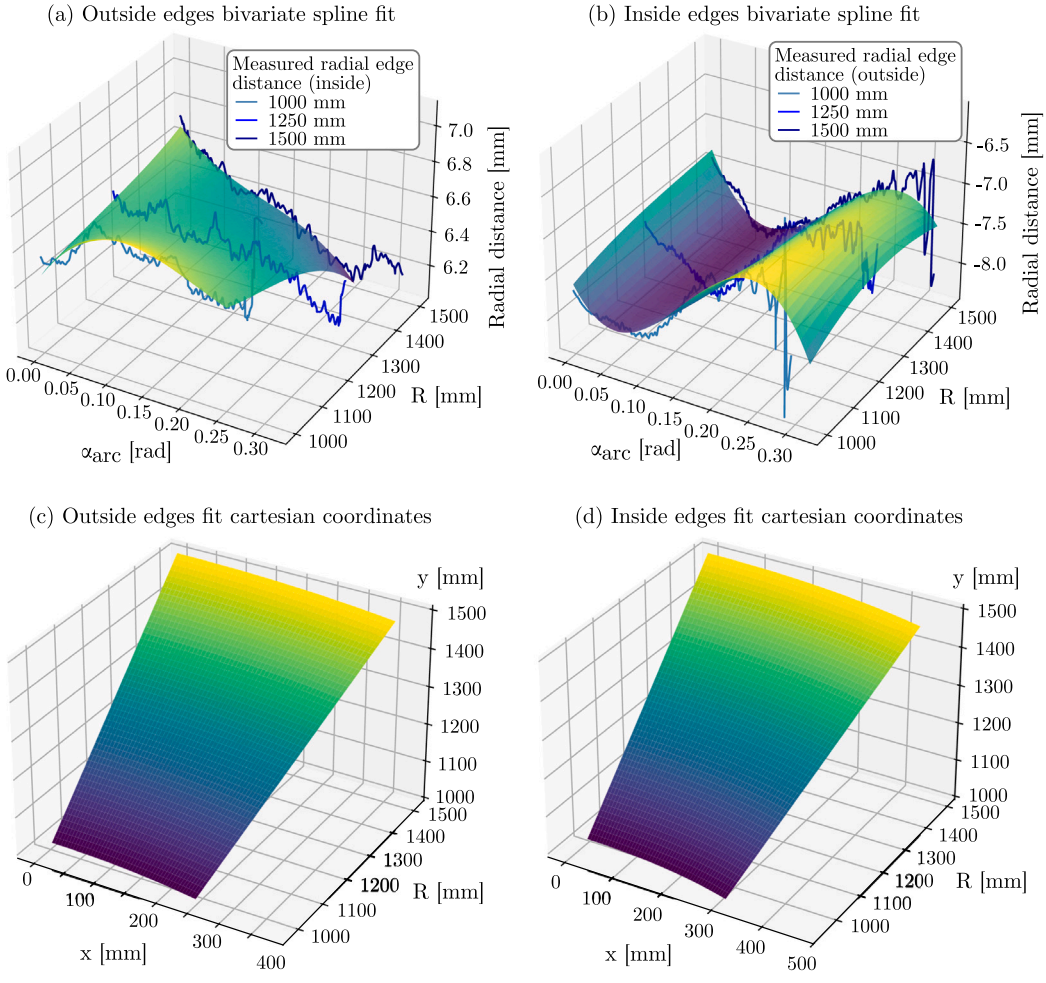

Fig. 9. Bivariate spline fits for average track edges of 1500 mm, 1250 mm and 1000 mm steering radii with half-inch tape.

Table 4
Bivariate spline fitting parameters and residuals.

	Half-inch spline fit		Quarter-inch spline fit	
	Outside edges	Inside edges	Outside edges	Inside edges
Smoothing factor s	1000	1000	1000	1000
Degrees k_x, k_y	3	3	3	3
Mean residual [mm]	0.00 ± 0.04	0.00 ± 0.08	0.00 ± 0.10	0.00 ± 0.08
Max residual [mm]	0.15	0.34	0.38	0.28

outer edge of the reference track and the inner edge of the subsequent track over the valid arc length based on the bivariate spline functions. The results of this optimization are presented in Fig. 10. For comparison, the radii of a parallel layup strategy, which correspond to reference radius plus consolidated tape width as would be the case in multiple-tow layup or standard AFP path planning, were added in the graphs. Additionally, a shifted strategy with the same radius as the reference radius and an optimized y-shift are also shown. For all reference radii and both tape widths, the fitted (optimized) radius of the subsequent track was smaller than in the shifted or parallel strategy. A linear correlation was, however, also observed between the reference input radii and the fitted subsequent track radii for both half-inch and quarter-inch tape (Fig. 10(a) and (c), respectively). The fitted radii for the half-inch and quarter-inch steering-optimized layup strategies exhibited a constant decrease of 22.5 ± 1.5 mm and 19.9 ± 1.1 mm, respectively.

A comparison of the optimized layup strategy with the standard parallel layup strategy and the shifted strategy with the same radius as the reference is presented in Fig. 10(b) and (d) for half-inch and quarter-inch tape, respectively. The average radial curve differences between the reference outer edge and the inner edge of the subsequent track of each layup strategy are presented to visualize the gap defect size between narrowing steered tapes of the three strategies. For both tape widths, the steering-optimized layup strategy achieved less than half the average radial distance observed with the parallel strategy. While the steering-optimized strategy provided only modest improvements over the shifted strategy for half-inch tape, a significant further reduction in radial curve deviation (less than 0.1 mm) was observed for quarter-inch tape. The optimized layup strategy thus presents a significant improvement over the standard parallel layup strategy with expected gap defects smaller than the standard deviation of the consolidated tape width of the straight reference tracks (Fig. 6).

4.3. Experimental validation of the optimized layup strategy

Fig. 11 presents validation examples for half-inch and quarter-inch steering plies beginning with a 1500 mm reference radius. Optimized steering curves were generated with maximum arc angles of 0.2 rad and 0.25 rad for the half-inch and quarter-inch tape, respectively, informed by the critical arc angle analysis. The resulting tape edge predictions demonstrate negligible deviation between the outer tape edges and the fitted inner tape edges (Fig. 11(a) and (c)).

The manufactured steering plies are shown in Fig. 11(b) and (d). Variation in the critical arc length resulted in shear defects and pronounced undulations along the inner tape edges of some tracks, leading to small gap defects. This effect was more pronounced in the half-inch ply compared to the quarter-inch ply. As anticipated, tow straightening was observed at the tape cut positions on the right-hand side.

Residual defects were characterized using optical 3D scanning data (Fig. 12). Deviations from optimal surface coverage were most prominent in the tow cut areas, resulting from tow straightening and transient process parameters which reduced the consolidated tape width. Section views A-A' and B-B' revealed smaller residual gaps at the inner tape edges of the half-inch and quarter-inch plies, respectively, attributed to in-plane undulations occurring below the critical arc length. Further reduction of the arc angle may mitigate these defects. Overall, the optimized layup strategy significantly minimized gap defects compared to conventional parallel layup.

The presented methodology was validated for a specific material, machine, and process parameter combination; however, the algorithm is readily trainable with empirical data from different setups. This includes different AFP machines, heat sources and prepreg tapes with other fiber types, fiber volume fractions and resin systems within the domain of thermoplastic in-situ AFP. Although the application for in-situ AFP makes the most sense, since the most accurate possible estimation of the consolidated tape geometry is important for path planning in order to avoid defects in the final component, an application for thermoset, dry fiber AFP or thermoplastic AFP with post-consolidation is also possible. Expanding the range of steering radii could potentially improve the accuracy of the spline fit and resulting layup paths. Currently, the algorithm is limited to constant curvature layup paths. Future work will explore non-constant curvature steering, potentially broadening the design space to applications such as linear variation reference curves or double-curved dome geometries. The algorithm is also limited to single-tow layup. As the individual tapes are inherently placed in parallel in multiple-tow AFP, the steering-induced gap defects between the narrowing individual tapes cannot be avoided. Although the gaps between the courses could be optimized, this would be of limited use as geometry-related gap defects between the courses are typically necessary for multiple-tow layup in order to comply with steering radius and fiber angle deviation boundary conditions. Single-tow tape placement with this optimization algorithm, however, could reduce the defects in components with complex curvatures to such an extent that in-situ consolidation could achieve sufficient component quality without the need for subsequent autoclave or press consolidation. All other AFP processes for the manufacture of steered composites come with limitations, as well. The novel technology of Continuous Tow Shearing, while able to manufacture very small steering radii without defects through a complete shear deformation mode, in its current iteration is limited to dry fiber placement and the end effector requires a flat contact area for the CTS module, which restricts its use in curved molds [9]. In thermoset AFP, the manufacturable steering radii are limited by the opposing effects of prepreg tack and out-of-plane buckling of the tape, allowing only for relatively large steering radii. Due to the complete consolidation, thermoplastic AFP can generally produce smaller radii without defects [11]. Without adjusting the layup strategy, the gap defects between narrowing tapes, however, impede the laminate quality. This work presents a solution for the manufacture of steered thermoplastic structures with minimal defects and thus extends the design space of the complex optimization problem in the selection of manufacturing processes, materials and laminate design parameters for the production of complex composite structures.

5. Conclusion

This work demonstrated a methodology for constant curvature steering based on an empirical model of tape geometry changes and a corresponding path planning algorithm, successfully validated for both half-inch and quarter-inch tapes. The approach is adaptable to different process parameters and machine-material combinations through training with relevant experimental data.

The combination of the critical arc length concept and optimized path planning provides a design space for high-quality, curved laminate fabrication using in-situ AFP. The defined envelope of usable steering parameters for the investigated material, process, and machine combination revealed greater design freedom for the quarter-inch material. This data serves as a foundation for process-optimized design for manufacturability of target components.

Future research will focus on characterizing the mechanical properties of steering laminates. Expanding the model to accommodate variable curvature will enable the design of more complex geometries, such as dome structures. Finally, further enhancing the tape guiding system to minimize fiber straightening at tape cuts and addressing transient effects at track starts and ends is crucial for achieving consistent layup quality throughout the laminate.

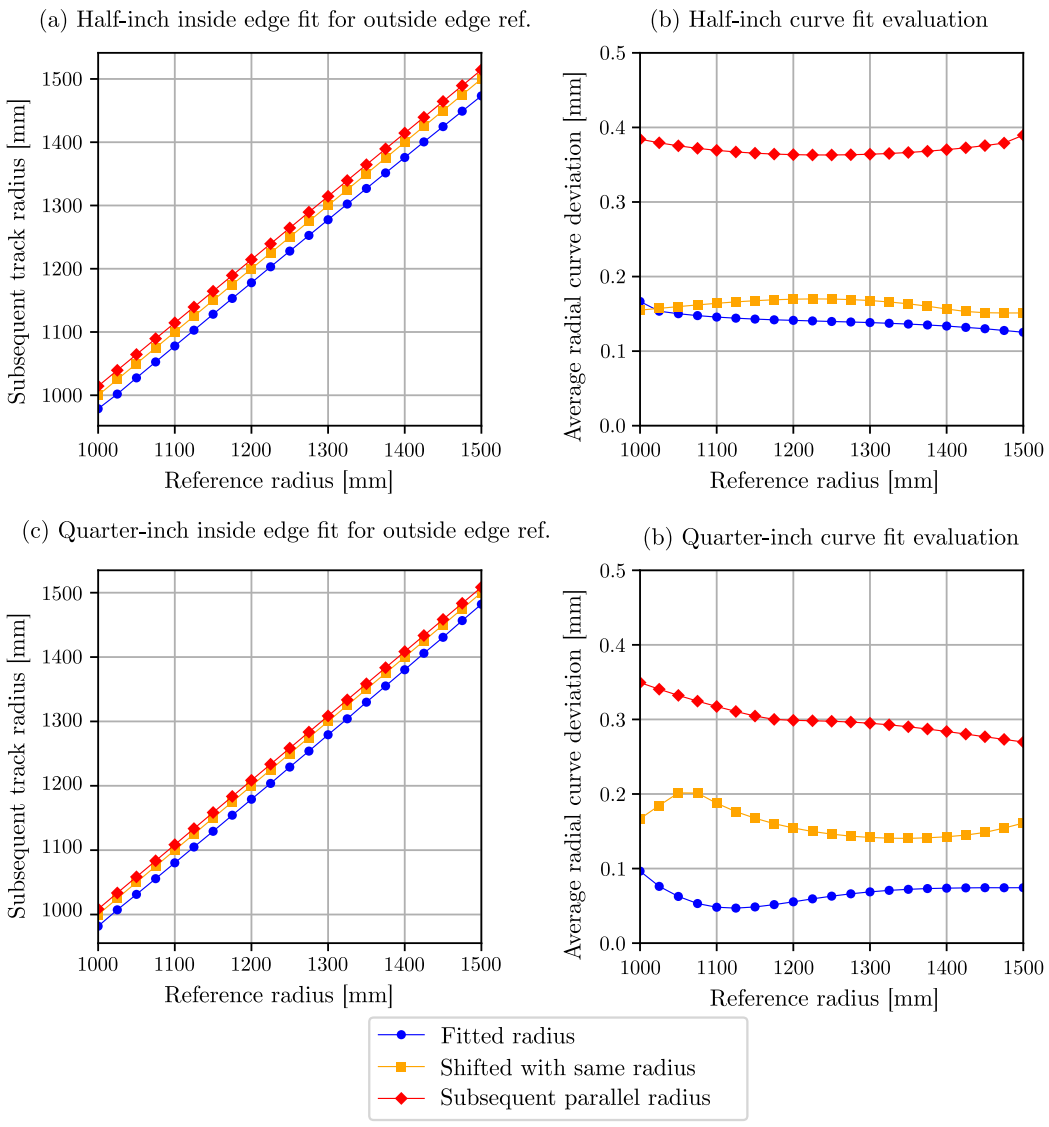

Fig. 10. Steering radius match and evaluation of curve fits.

CRediT authorship contribution statement

Lukas Raps: Writing – original draft, Visualization, Validation, Methodology, Investigation, Formal analysis, Data curation, Conceptualization. **Ashley R. Chadwick:** Writing – review & editing, Supervision, Methodology. **Yannick Schäfer:** Methodology, Investigation. **Heinz F. Voggenreiter:** Writing – review & editing, Supervision, Resources, Funding acquisition.

Declaration of competing interest

The authors declare that they have no known competing financial interests or personal relationships that could have appeared to influence the work reported in this paper.

Acknowledgments

This research work is part of the project FFS (Fortschrittliche Flugzeugstrukturen) which is financially supported by the German Federal Ministry of Defence.

Appendix

Half-inch outside edge bivariate spline coefficients:
Knot vector T_x = [$2.78951e^{-14}$, $2.78951e^{-14}$, $2.78951e^{-14}$, $2.78951e^{-14}$, 0.249939, 0.249939, 0.249939, 0.249939]
Knot vector T_y =[1000, 1000, 1000, 1000, 1500, 1500, 1500, 1500]
2D B-spline coefficients: [6.45582, 6.54539, 6.54539, 6.669, 6.98806, 6.45912, 6.45912, 6.29628, 6.71699, 6.51175, 6.51175, 6.4396, 6.58677, 6.45109, 6.45109, 6.02875]

Half-inch inside edge bivariate spline coefficients:
Knot vector T_x = [$-1.70108e^{-12}$, $-1.70108e^{-12}$, $-1.70108e^{-12}$, $-1.70108e^{-12}$, 0.318275, 0.318275, 0.318275, 0.318275]
Knot vector T_y =[1000, 1000, 1000, 1000, 1500, 1500, 1500, 1500]
2D B-spline coefficients: [−7.59577, −7.3603, −7.3603, −7.31099, −9.24179, −9.63879, −9.63879, −9.56711, −5.28991, −5.88401, −5.88401, −6.20487, −7.67588, −7.25631, −7.25631, −7.49023]

Quarter-inch outside edge bivariate spline coefficients:
Knot vector T_x = [$1.10612e^{-12}$, $1.10612e^{-12}$, $1.10612e^{-12}$, $1.10612e^{-12}$, 0.249939, 0.249939, 0.249939, 0.249939]

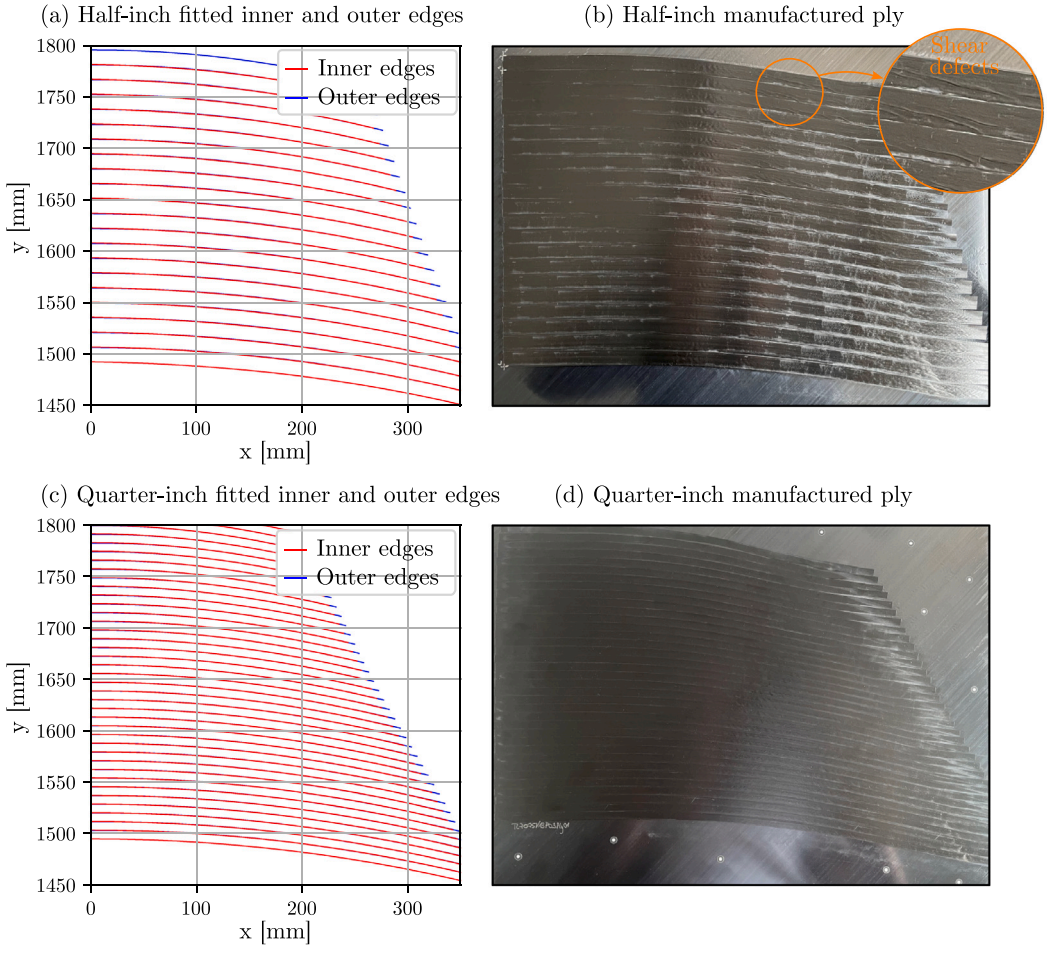

Fig. 11. Optimized example steering plies and manufactured validation plies.

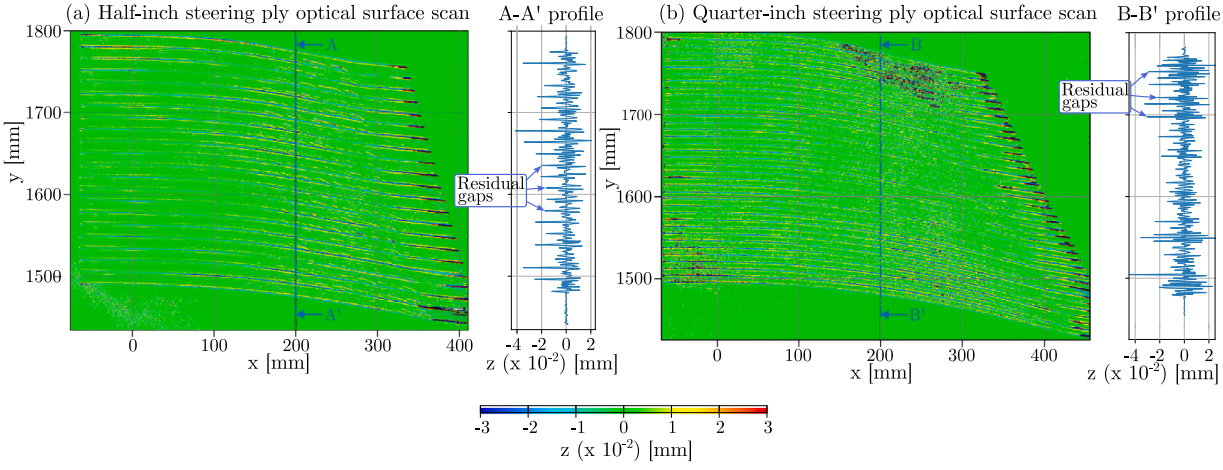

Fig. 12. Optical 3D scans of steering plies.

Knot vector T_y =[1000, 1000, 1000, 1000, 2000, 2000, 2000, 2000]
2D B-spline coefficients: [3.0756, 3.51888, 3.18803, 3.67935, 3.85118, 4.33503, 4.61062, 4.19819, 3.18508, 3.78765, 3.11964, 3.77772, 3.97662, 3.74949, 4.4902, 3.59517]

Quarter-inch inside edge bivariate spline coefficients:
Knot vector T_x = [0.000628381, 0.000628381, 0.000628381, 0.000628381, 0.25418, 0.25418, 0.25418, 0.25418]
Knot vector T_y =[1000, 1000, 1000, 1000, 2000, 2000, 2000, 2000]
2D B-spline coefficients: [−4.89414, −5.39781, −4.22882, −4.80241, −4.86876, −5.02925, −4.66134, −4.91733, −4.85568, −3.07546, −4.93219, −3.71276, −3.76164, −4.07977, −3.54249, −4.36585]

Data availability

Data will be made available on request.

References

[1] Chadwick AR, Doll G, Christ U, Maier S, Lansky S. Performance of in-situ automated fibre placement parts. Compos A 2025;192:108725.
[2] Blom AW. Structural performance of fiber-placed, variable-stiffness composite conical and cylindrical shells [Ph.D. thesis], 2010.
[3] Smith RP, Qureshi Z, Scaife RJ, El-Dessouky HM. Limitations of processing carbon fibre reinforced plastic/polymer material using automated fibre placement technology. J Reinf Plast Compos 2016;35(21):1527–42.
[4] Peeters DMJ, Lozano GG, Abdalla MM. Effect of steering limit constraints on the performance of variable stiffness laminates. Comput Struct 2017;196:94–111.
[5] Bakhshi N, Hojjati M. An experimental and simulative study on the defects appeared during tow steering in automated fiber placement. Compos A 2018;113:122–31.
[6] Kim BC, Hazra K, Weaver P, Potter K. Limitations of fibre placement techniques for variable angle tow composites and their process-induced defects. In: Proceedings of the 18th international conference on composite materials. ICMM18, Jeju, Korea; 2010, p. 21–6.
[7] Kim BC, Potter K, Weaver PM. Continuous tow shearing for manufacturing variable angle tow composites. Compos A 2012;43(8):1347–56.
[8] Kim BC, Weaver PM, Potter K. Manufacturing characteristics of the continuous tow shearing method for manufacturing of variable angle tow composites. Compos A 2014;61:141–51.
[9] Rautmann M, Gabriel ER, Kim BC. Advanced continuous tow shearing process utilising in-line tow width control in fibre steering. Compos A 2025;196:109025.
[10] Oliveri V, Zucco G, Peeters D, Clancy G, Telford R, Rouhi M, McHale C, O'Higgins RM, Young TM, Weaver PM. Design, manufacture and test of an in-situ consolidated thermoplastic variable-stiffness wingbox. AIAA J 2019;57(4):1671–83.
[11] Clancy G, Peeters D, Oliveri V, Jones D, O'Higgins RM, Weaver PM. A study of the influence of processing parameters on steering of carbon fibre/PEEK tapes using laser-assisted tape placement. Compos B 2019;163:243–51.
[12] Rajasekaran A, Shadmehri F. Steering of carbon fiber/PEEK tapes using hot gas torch-assisted automated fiber placement. J Thermoplast Compos Mater 2022;08927057211067962.
[13] Zenker T, Gnaedinger M. Consolidation behavior of fiber steered thermoplastic automated fiber placement preforms. In: 5th international conference & exhibition on thermoplastic composites. 2020.
[14] Zenker T. Einfluss prozessspezifischer designparameter des thermoplastischen automated fiber placements auf die bauteilqualität in abhängigkeit der prozesskette [Ph.D. thesis], 2022.
[15] Wang H, Chen J, Fan Z, Xiao J, Wang X. Experimental investigation on the influence of fiber path curvature on the mechanical properties of composites. Comput Struct 2021;14(10):2602.
[16] Schwab ZenkerThomasund, M. Analysis of fiber steering effects in thermoplastic automated fiber placement. In: ECCM18-18th European conference on composite materials. 2018.
[17] Raps L, Chadwick AR, Schiel I, Schmidt I. CF/LM-PAEK: characterisation and sensitivity to critical process parameters for automated fibre placement. Compos Struct 2022;284:115087.